

Cite this: *Chem. Sci.*, 2024, 15, 7757

All publication charges for this article have been paid for by the Royal Society of Chemistry

Photochemical and biological dual-effects enhance the inhibition of photosensitizers for tumour growth†

Huiyu Niu,^a Yang Liu,^a Yafu Wang,^a Yonggang Yang,^a Ge Wang,^d Tony D. James,^{ac} Jonathan L. Sessler^{id}*^b and Hua Zhang^{id}*^a

Photosensitizers typically rely on a singular photochemical reaction to generate reactive oxygen species, which can then inhibit or eradicate lesions. However, photosensitizers often exhibit limited therapeutic efficiency due to their reliance on a single photochemical effect. Herein, we propose a new strategy that integrates the photochemical effect (type-I photochemical effect) with a biological effect (proton sponge effect). To test our strategy, we designed a series of photosensitizers (ZZ-sers) based on the naphthalimide molecule. ZZ-sers incorporate both a *p*-toluenesulfonyl moiety and weakly basic groups to activate the proton sponge effect while simultaneously strengthening the type-I photochemical effect, resulting in enhanced apoptosis and programmed cell death. Experiments confirmed near-complete eradication of the tumour burden after 14 days ($W_{\text{light}}/W_{\text{control}} \approx 0.18$, W represents the tumour weight). These findings support the notion that the coupling of a type-I photochemical effect with a proton sponge effect can enhance the tumour inhibition by ZZ-sers, even if the basic molecular backbones of the photosensitizers exhibit nearly zero or minimal tumour inhibition ability. We anticipate that this strategy can be generalized to develop additional new photosensitizers with improved therapeutic efficacy while overcoming limitations associated with systems relying solely on single photochemical effects.

Received 5th February 2024
Accepted 25th April 2024

DOI: 10.1039/d4sc00874j

rsc.li/chemical-science

Introduction

Photosensitizers are typically based on a single effect, *i.e.* the photochemical effect in the PDT process, which generates potent oxidizing substances, such as superoxide radicals ($\text{O}_2^{\cdot-}$), singlet oxygen ($^1\text{O}_2$) and other reactive oxygen species (ROS) through an electron transfer (type-I PDT) or energy transfer (type-II PDT) at a tumour site under the action of oxygen and a light source.^{1–5} Therefore, successful implementation of traditional PDT generally depends on three essential elements, a photosensitizer, oxygen, and a source of light.^{2,6} The absence of just one of these three essential elements will inevitably

result in a significant reduction or even complete loss of the PDT effect.⁷ Moreover, both the lifetime (0.03–0.18 ms) and action distance (0.01–0.02 μm) of the generated ROS (*e.g.*, $^1\text{O}_2$, $\text{O}_2^{\cdot-}$, *etc.*) are limited,^{8–10} which can result in another crucial limitation of PDT. There is thus a need for new strategies that can enhance the function of photosensitizers and which can address the deficiencies of PDT.

To date, many photosensitizers have been developed using different functional enhancement strategies. Near-infrared I, II and up-conversion designs based on boron-dipyrromethene (BODIPY) and cyanine derived photosensitizers have been utilized to compensate for the low tissue penetration associated with visible excitation light sources.^{11–13} To reduce the oxygen dependence associated with PDT, efforts have been made to change the underlying photochemical reactions from type-II to type-I.¹⁴ For instance, a self-assembly strategy was used to stabilize fluorescein in the charge separated (CS) state thus switching the system from type-II PDT in the monomer state to type-I PDT after self-assembly.¹⁵ Moreover, to address the problem of the oxygen dependence of PDT, an oxygen-independent photosensitizer that generates hydroxyl radicals ($\cdot\text{OH}$) by oxidizing water in the presence of pyruvate was prepared.¹⁶ While these approaches are promising for overcoming difficulties associated with low light fluxes or reduced oxygen, these do not address problems associated with limited

^aKey Laboratory of Green Chemical Media and Reactions, Ministry of Education, Collaborative Innovation Centre of Henan Province for Green Manufacturing of Fine Chemicals, Organic Functional Molecules and Drug Innovation Key Laboratory of Henan Province, School of Chemistry and Chemical Engineering, Henan Normal University, Xinxiang, Henan 453007, P. R. China. E-mail: zhh1106@htu.edu.cn; Fax: +86-373-3329030; Tel: +86-373-3329030

^bDepartment of Chemistry, The University of Texas at Austin, Austin, 78712, USA. E-mail: sessler@cm.utexas.edu

^cDepartment of Chemistry, University of Bath, Bath, BA2 7AY, UK

^dCollege of Basic Medicine, Xinxiang Medical University, Xinxiang, Henan 453007, P. R. China

† Electronic supplementary information (ESI) available. See DOI: <https://doi.org/10.1039/d4sc00874j>



ROS lifetimes or action distances. To address these latter needs, efforts are being made to create photosensitizers that promote additional biological effects, including those associated transmembrane transport, proton sponge effect, and oxidative stress, among others.^{17–20} For example, metal nanoparticles such as TiO₂ that promote transmembrane transport have been used for drug delivery.¹⁷ Separately, amino-functionalized polymers that rely on the so-called proton sponge effect that causes lysosomes to rupture due to protonation have shown promise in treating various diseases.¹⁹ These strategies are based on biological effects that general operate by mechanisms distinct from those involved in PDT. We thus considered it likely that new photosensitizers that integrate both classic photochemical effects and these biological modalities would allow the deficiencies inherent in a single-effect PDT system to be overcome. The present study was designed to test the merits of this hypothesis.

With the above goal in mind, we developed a series of photosensitizers (**ZZ-sers**, Fig. 1). These agents were designed to couple photochemical and biological effects within a single action system. A type-I photochemical effect provides one component of this putative dual action system, while a proton sponge effect, designed to induce lysosomal membrane instability and trigger apoptosis through the release of lysosomal contents into the cytoplasm^{21–26} was used as the second component. To test the feasibility of this strategy and assess the enhanced tumour inhibition effects, naphthalimide, a classic two-photon system that typically exhibits limited PDT efficacy, was chosen as the basic skeleton for the **ZZ-sers** series. The D- π -A molecular backbone in the **ZZ-sers** was designed to facilitate effective intersystem crossing (ISC) and enhance the conversion efficiency from S₁ to T₁.^{27–29} Furthermore, it was expected that two-photon photosensitizing activity would be instigated upon irradiation with a long wavelength light source,

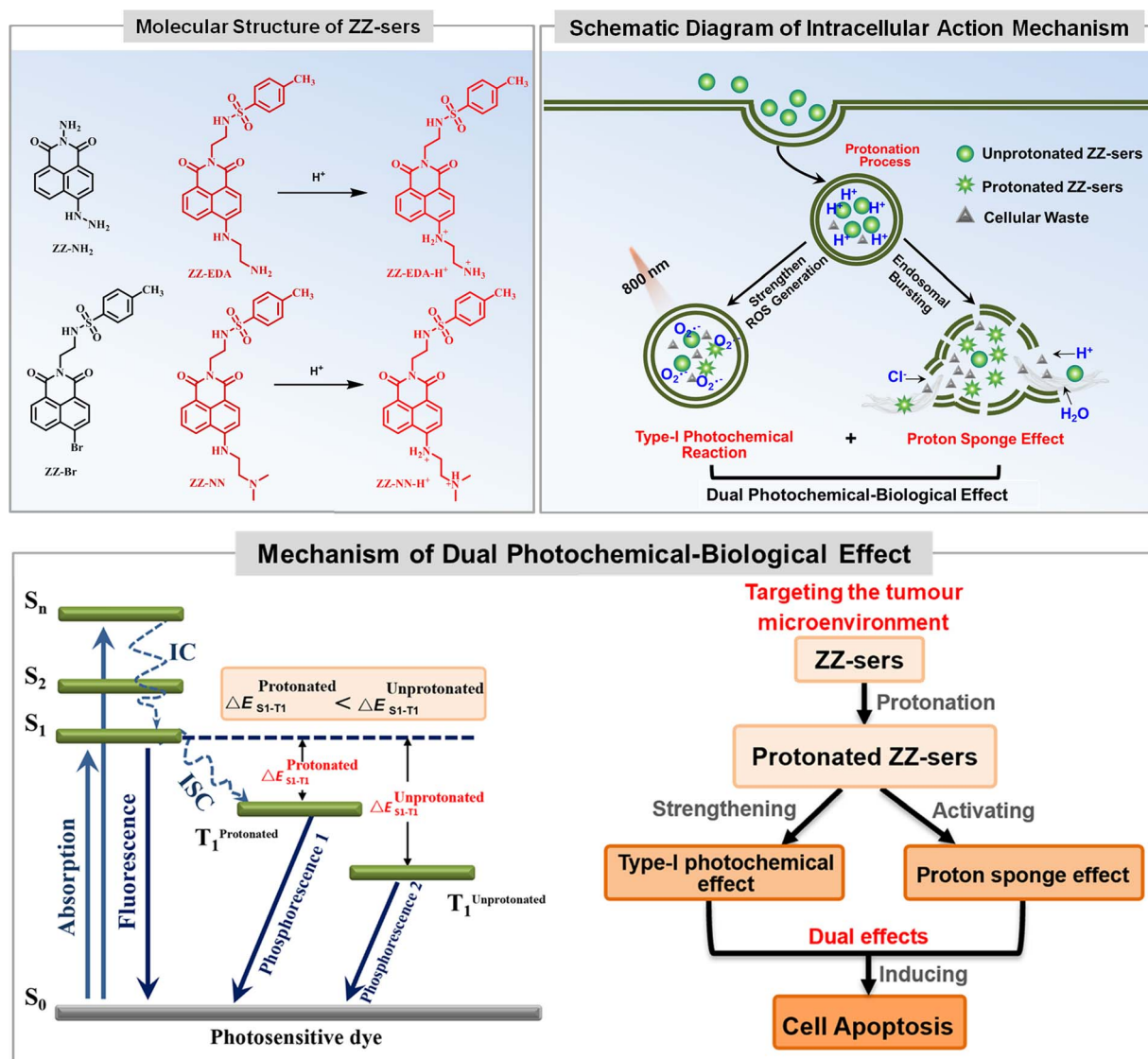


Fig. 1 Molecular structures of photosensitizers (ZZ-Br, ZZ-NH₂, ZZ-NN and ZZ-EDA) and mechanism of the proposed dual photochemical-biological approach that underlies the present study.



such as a pulsed laser. Targeting for lysosomes and an improved proton sponge effect *in situ*, was expected based on the introduction of weakly basic groups, such as ethylenediamine and *N,N*-dimethylethylenediamine, to the 4-position of the naphthalimide.³⁰ Furthermore, to enhance the charge separation efficiency, a *p*-toluenesulfonyl group was introduced to the N atom at the “top” of the naphthalimide to give **ZZ-EDA**, **ZZ-NN**, **ZZ-EDA-H⁺** and **ZZ-NN-H⁺**, respectively. Two control compounds, **ZZ-Br** and **ZZ-NH₂** were also prepared. The corresponding synthetic routes and experimental details are provided in Scheme S1.† Nuclear magnetic resonance (NMR) spectroscopy and mass spectrometry (MS) data for all the new compounds were consistent with the proposed structures (*cf.* Fig. S1–S13†). All characterization data is included in the ESI.† Preliminary studies revealed that **ZZ-EDA**, **ZZ-NN**, **ZZ-EDA-H⁺** and **ZZ-NN-H⁺** behaved similarly. Therefore, **ZZ-NN** and **ZZ-NN-H⁺** were used as representative examples and subject to detailed evaluation.

Results and discussion

Analysis in solution

The photochemical behavior of the photosensitizers (**ZZ-EDA** and **ZZ-NN**), protonated photosensitizers (**ZZ-EDA-H⁺** and **ZZ-NN-H⁺**) and control compounds (**ZZ-Br** and **ZZ-NH₂**) were initially evaluated in solution. The pK_a values of **ZZ-EDA** and **ZZ-NN** were determined to be 8.07 and 7.15 (Fig. 2a and S16†) respectively. The data indicated that **ZZ-EDA** and **ZZ-NN** could be protonated at pH 5.0 to form protonated photosensitizers (**ZZ-EDA-H⁺** and **ZZ-NN-H⁺**, Fig. 1), which was also evidenced by the NMR data (Fig. S14†) and TLC analysis (Fig. S23c†). Such protonation behaviour is conducive to the activation of the proton sponge effect. To elucidate the excited singlet state-triplet state of **ZZ-EDA**, **ZZ-NN**, **ZZ-EDA-H⁺** and **ZZ-NN-H⁺**, their absorption, fluorescence and phosphorescence spectra were recorded (Fig. S15†). Using **ZZ-NN** as a representative molecule, these studies revealed a prominent absorption peak at 436 nm ($\lambda_{\text{ex}}^{\text{one-photon}}$, Fig. S15d†) characterized by high molar extinction coefficients ($\epsilon_{\text{ZZ-NN-H}^+} = 11637.5 \text{ M}^{-1} \text{ cm}^{-1}$, $\epsilon_{\text{ZZ-NN}} = 12585.5 \text{ M}^{-1} \text{ cm}^{-1}$, Table 1). The data indicated that **ZZ-NN** and **ZZ-NN-H⁺** exhibited excellent photon capture ability. Significantly, **ZZ-NN** also exhibits a two-photon absorption at 800 nm ($\lambda_{\text{ex}}^{\text{two-photon}}$, Fig. S26†), leading us to infer that excitation by long-wavelength pulsed lasers would be feasible. Fluorescence signals were generated at 532 nm with quantum yields of $\Phi_{\text{ZZ-NN-H}^+} = 0.53$ and $\Phi_{\text{ZZ-NN}} = 0.39$ (Fig. S15e† and Table 1) when excited at 438 nm. Additionally, **ZZ-NN** exhibited prolonged phosphorescence lifetimes after protonation ($\tau_{\text{ZZ-NN-H}^+} = 265.08 \text{ ms}$, $\tau_{\text{ZZ-NN}} = 217.65 \text{ ms}$, Fig. 2b and Table 1). These observations provide support for the notion that these dyes, once excited, can persist in the triplet state for an extended time, thus allowing energy or electron transfer under conditions of PDT.³¹ Taken in concert, these results demonstrate that both **ZZ-NN** and **ZZ-NN-H⁺** exhibit exceptional photophysical properties. Moreover, the photophysical properties of **ZZ-NN-H⁺** surpass those of **ZZ-NN**. As such we propose that the protonation of **ZZ-NN** at pH 5.0 has the potential to enhance the photochemical effects. For

comparison, **ZZ-EDA** and **ZZ-EDA-H⁺** also exhibit similar photophysical properties (Fig. S15–S18†).

Good light-stability is crucial for efficient photosensitizers.¹⁴ Therefore, we evaluated the optical stability of **ZZ-EDA**, **ZZ-EDA-H⁺**, **ZZ-NN** and **ZZ-NN-H⁺** in solution ($V_{\text{buffer}} : V_{\text{methanol}} = 2 : 1$). The fluorescence intensity of both **ZZ-EDA**, **ZZ-EDA-H⁺**, **ZZ-NN** and **ZZ-NN-H⁺** remained unchanged (Fig. S16†) under continuous 5 h irradiation (iodine-tungsten lamp, 500 W), ensuring that any signal changes observed during subsequent ROS monitoring could be attributed to ROS generated by the photosensitive dye under irradiation. Then, the electron paramagnetic resonance (EPR) spectrum was used to determine the ROS production of **ZZ-EDA**, **ZZ-NN** and the control molecules (**ZZ-Br** and **ZZ-NH₂**). The results indicated that only the characteristic peak of $\text{O}_2^{\cdot-}$ appears in the EPR spectra of **ZZ-NN** (Fig. 2c), **ZZ-EDA** (Fig. S22†), **ZZ-Br** and **ZZ-NH₂** (Fig. S22†). While no characteristic peaks for $^1\text{O}_2$ were observed. Then, 9,10-anthracenediyl-bis (methylene) dimalonic acid (ABDA, an indicator for $^1\text{O}_2$) and dihydroethidium (DHE, an indicator for $\text{O}_2^{\cdot-}$) were used to further determine the ROS generation of the **ZZ-sers** in solution.^{1,32,33} For ABDA in the presence of **ZZ-sers** and light-irradiation, the absorbance changes were negligibly (Fig. S19†). However, as shown in Fig. S19,† obvious fluorescence enhancements of DHE were observed in the presence of **ZZ-NH₂**, **ZZ-EDA** and **ZZ-NN** under illumination. These findings collectively validate that **ZZ-sers** predominantly generate $\text{O}_2^{\cdot-}$ through a type-I photochemical process when subjected to a brief period of irradiation. To further investigate the impact of protonation on the photochemical effects, dihydrorhodamine 123 (DHR 123) was also used to evaluate the $\text{O}_2^{\cdot-}$ production capacity of **ZZ-NN**, **ZZ-NN-H⁺**, **ZZ-EDA**, **ZZ-EDA-H⁺** and the control molecules (**ZZ-Br** and **ZZ-NH₂** in solutions of $V_{\text{buffer}} : V_{\text{methanol}} = 2 : 1$ with pH = 5.0 or 7.2).¹ The results (Fig. 2d and S20†) indicate that **ZZ-Br** and **ZZ-NH₂** showed a relatively weak $\text{O}_2^{\cdot-}$ generation ability compared to **ZZ-NN** and **ZZ-EDA**. Moreover, **ZZ-NN-H⁺** exhibits higher $\text{O}_2^{\cdot-}$ generation ($F/F_0 = 39.96$, after 80 s of irradiation) compared to **ZZ-NN** ($F/F_0 = 24.56$, Fig. 2d). This can be attributed primarily to the protonation of the amino group³⁴ and increased charge separation efficiency, which facilitates ISC and electron transfer in the triplet state.²⁶ **ZZ-EDA** and **ZZ-EDA-H⁺** with a similar structure exhibited photochemical reactions and features (Fig. S19, S21 and S22†) analogous to those of **ZZ-NN** and **ZZ-NN-H⁺**. Therefore, protonation can also augment the photochemical effects of **ZZ-EDA**. Whereas, under the same condition, the $\text{O}_2^{\cdot-}$ generation rate of **ZZ-NN-H⁺** were higher than that of **ZZ-EDA-H⁺** (Fig. S21†) which may be due to the greater protonation ability of **ZZ-NN**.

Mechanistic studies

The above results provide support for the suggestion that **ZZ-NN** and **ZZ-EDA** will exhibit dual photochemical-biological effects under conditions of photo-irradiation. To provide a stronger foundation for this hypothesis, an electron-hole analysis was conducted, and the degree of charge separation was evaluated using the *t* index (where *t* is a measure of the degree of



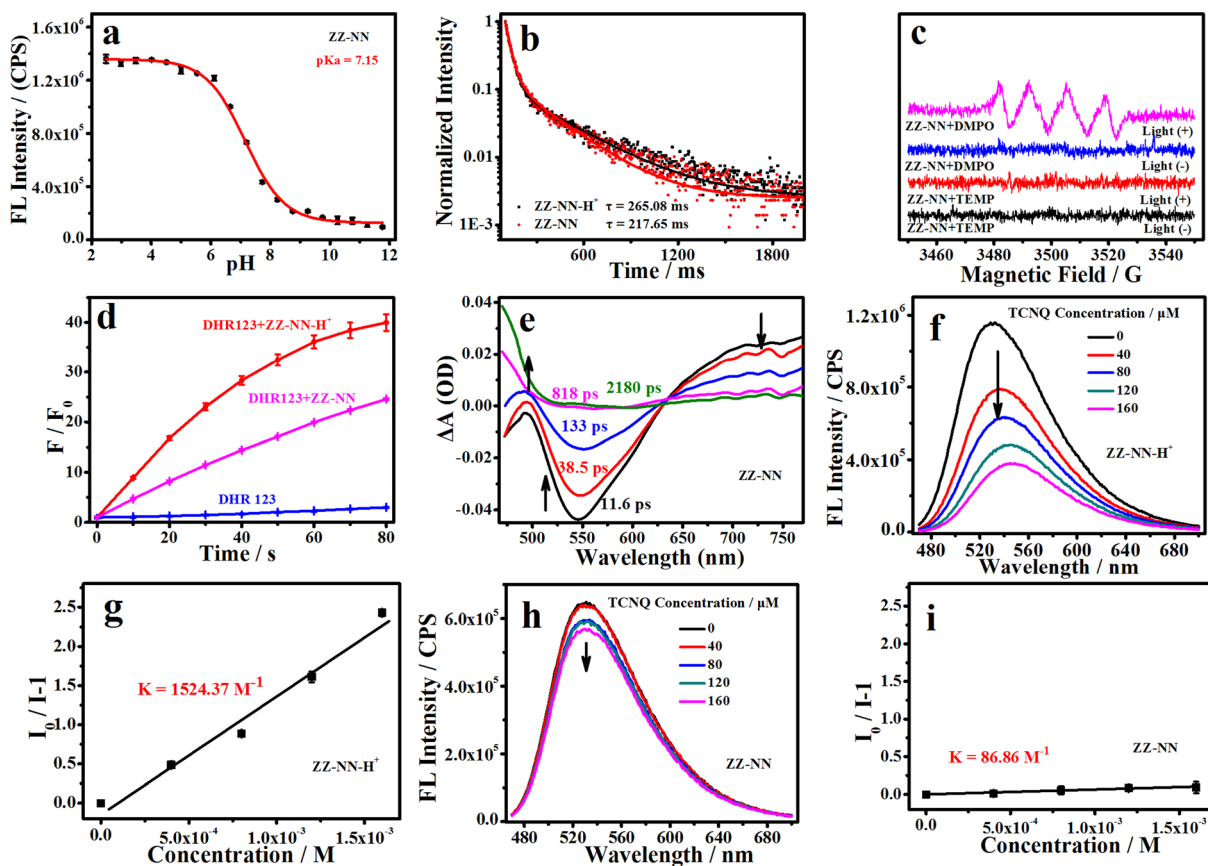


Fig. 2 (a) Change in the fluorescence intensity of ZZ-NN (3.0 μM) at the maximum emission (537 nm) as a function of pH as recorded in mixed buffer–methanol solutions ($V_{\text{buffer}} : V_{\text{methanol}} = 2 : 1$) over the pH 2–12 range. (b) Phosphorescence attenuation curves for ZZ-NN (20 μM, $\lambda_{\text{em}} = 535$ nm) and ZZ-NN-H⁺ (20 μM, $\lambda_{\text{em}} = 535$ nm). (c) Electron paramagnetic resonance (EPR) spectra of ZZ-NN with and without light irradiation (2,2,6,6-tetramethylpiperidine (TEMP), a trapping agent for $^1\text{O}_2$; 5,5-dimethyl-1-pyrroline N-oxide (DMPO), a trapping agent for $\text{O}_2^{\cdot-}$). (d) Changes in fluorescence intensity of DHR 123 (20 μM, an indicator for $\text{O}_2^{\cdot-}$) seen in the presence of ZZ-NN (20 μM) and ZZ-NN-H⁺ (20 μM) when subject to irradiation at 800 nm for different times; here, a femtosecond pulsed laser is used to achieve the two-photo excitation, 9.15 mW cm^{-2}). (e) Femtosecond transient absorption spectra of ZZ-NN (1.0 mM in DMSO, $\lambda_{\text{ex}} = 445$ nm). (f) Changes in fluorescence intensity of ZZ-NN-H⁺ induced by different concentrations of 7,7,8,8-tetracyanoquinodimethane (TCNQ, 0–160 μM). (g) Stern–Volmer plots generated from the fluorescence intensity of ZZ-NN-H⁺ (20 μM) measured in the presence of increasing concentrations of TCNQ (0–160 μM). (h) Changes in fluorescence intensity for a sample of ZZ-NN induced via the addition of different concentrations of TCNQ (0–160 μM). (i) Stern–Volmer plots generated from the fluorescence intensity of ZZ-NN (20 μM) measured in the presence of increasing concentrations of TCNQ (0–160 μM).

separation between holes and electrons).²⁷ The t index of ZZ-NN proved to be 0.118 (Table 2), indicating a significant degree of charge separation (Fig. 3). ZZ-EDA was also found to exhibit a positive t index ($t = 0.281$). The ability to separate charge is expected to correlate in a positive way with an enhanced ISC and effective electron transfer efficiency in these two systems. In contrast to what was seen for ZZ-NN and ZZ-EDA, little evidence

of charge separation was seen for ZZ-Br ($t = -1.055$) and ZZ-NH₂ ($t = -0.060$) (Fig. 3 and Table 2). The energy level differences ($\Delta E_{\text{S}_1-\text{T}_1}$) from S_1 to T_1 of ZZ-NN were calculated using Gaussian B3LYP/TZVP, and a value of $\Delta E_{\text{S}_1-\text{T}_1}$ of 0.65 eV was obtained (Fig. 3 and Table 2). Therefore, we conclude that the effective ISC inferred on the basis of the t index values is thermodynamically favorable. Furthermore, the femtosecond transient

Table 1 Photophysical properties of ZZ-EDA, ZZ-EDA-H⁺, ZZ-NN and ZZ-NN-H⁺

	Solution pH ^a	$\lambda_{\text{ex/em-FL}}$ ^b (nm)	ϵ (M ⁻¹ cm ⁻¹)	Φ_{FL} ^c (%)	τ_{FL} ^d (ns)	$\lambda_{\text{em-PL}}$ ^e (nm)	τ_{PL} ^f (ms)
ZZ-EDA-H ⁺	5.00	435/533	8680	54.34	8.81	535	298.35
ZZ-EDA	7.20	435/533	9573.5	48.92	8.67	540	295.75
ZZ-NN-H ⁺	5.00	432/527	11 637.5	53.43	9.06	534	265.08
ZZ-NN	7.20	436/525	12 585.5	39.25	8.87	532	217.65

^a Note, $V_{\text{pHbuffer}} : V_{\text{methanol}} = 2 : 1$. ^b Maximum absorption wavelength and fluorescence emission wavelength. ^c Fluorescence quantum yield. ^d Fluorescence lifetime. ^e Maximum phosphorescence emission wavelength. ^f Phosphorescence lifetime.

Table 2 Results of electron hole and triplet level analyses^a

	Sr	D	H	t	HDI	EDI	$\Delta E_{S_1-T_1}$ (eV)
ZZ-NH₂	0.657	1.78	2.75	-0.060	9.11	7.30	0.740
ZZ-Br	0.817	0.927	2.84	-1.055	6.92	7.05	1.14
ZZ-NN	0.641	1.98	2.88	0.118	8.86	7.30	0.650
ZZ-NN-H⁺	0.070	7.26	2.18	5.846	19.13	7.64	0.020
ZZ-EDA	0.646	1.86	2.79	0.281	9.06	7.30	0.650
ZZ-EDA-H⁺	0.090	4.78	2.07	3.634	19.68	7.73	0.050

^a Note, t : measure the degree of separation between holes and electrons. $t > 0$, implies that holes and electrons are sufficiently separated by charge transfer, while t values < 0 indicate a lack of appreciable separation between the holes and electrons along the charge transfer direction. Sr: the average overlap level of holes and electrons. D : the distance between the centroids of hole and the electron. H : the overall average distribution of holes and electrons. HDI: hole delocalization index. EDI: electron delocalization index. The D index is small, the t index is obviously negative, and the Sr is large, which is consistent with the formation of a locally excited state.

absorption spectrum (Fig. 2e) exhibited positive signals near 479 nm, which can be attributed to the triplet state. 7,7,8,8-Tetracyanoquinodimethane (TCNQ) quenching experiments³⁵ were also performed, and the quenching constants³⁶ ($K_{ZZ-NN} = 86.86 \text{ M}^{-1}$, Fig. 2h and i) provided support for the notion that an electron transfer process occurs in **ZZ-NN** following photo-excitation. The resulting charge separation is thought to support the production of $\text{O}_2^{\cdot-}$ via the T_1 state through electron transfer, *i.e.*, type-I PDT.

To determine the impact of protonation on the overall mechanism, the electron hole (Fig. S23a[†]) and electron transfer ability of **ZZ-NN-H⁺** was monitored under acidic conditions designed to mimic the tumour microenvironment. Following protonation, the t index of **ZZ-NN-H⁺** (Table 2) was found to be 5.846. This was taken as evidence that **ZZ-NN-H⁺** is better able to support charge separation than **ZZ-NN** ($t = 0.118$). In other words, **ZZ-NN-H⁺** exhibits higher susceptibility to ISC and electrontransfer than **ZZ-NN**. The $\Delta E_{S_1-T_1}$ value for **ZZ-NN-H⁺** was calculated to be 0.020 eV (Fig. S23b[†]). This value is expected to correlate with an enhanced ISC effect compared to **ZZ-NN**. Quenching experiments with TCNQ confirmed that a greater level of electron transfer occurs in the case of **ZZ-NN-H⁺** ($K_{ZZ-NN-H^+} = 1524.37 \text{ M}^{-1}$, Fig. 2f and g) than **ZZ-NN**. These findings align with our previous observations regarding the $\text{O}_2^{\cdot-}$ production capacity of **ZZ-NN** and **ZZ-NN-H⁺** (Fig. 2d).

Therefore, **ZZ-NN** can initiate a proton sponge effect through a protonation process to form **ZZ-NN-H⁺**. This system also engenders photochemical effects, resulting in a dual photochemical-biological effect. Given its structural similarity to **ZZ-NN**, we suggest that similar beneficial dual photochemical-biological effects may be seen in the case of **ZZ-EDA** (Fig. S23 and S24[†]).

Analysis in cells

To determine if the proposed dual photochemical-biological effects would lead to benefits in living cells, the HepG2 and 4T1 cell lines were selected to evaluate the putative PDT benefits of **ZZ-sers** at the cellular level. First, the cytotoxicity of **ZZ-sers** was determined using a standard methyl thiazolyte-trazolium (MTT) assay. As codified in Fig. 4, **ZZ-NN** and **ZZ-EDA** have little effect on the cell viability of HepG2 and 4T1 cells in the control group (*i.e.*, in the absence of photo-irradiation). However, when subject to photo-excitation both **ZZ-NN** and **ZZ-EDA** were found to inhibit the proliferation of HepG2 and 4T1 cells and in a concentration-dependent manner. Cell viabilities of $48.37\% \pm 0.30\%$ and $35.33\% \pm 0.23\%$ were seen upon incubation with **ZZ-EDA** (5.0 μM). **ZZ-NN** produced cell

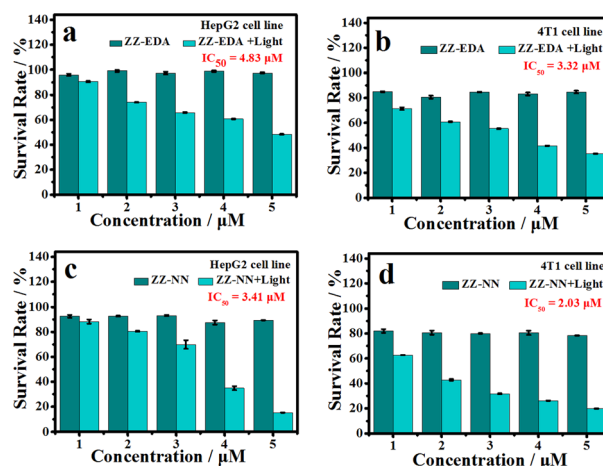


Fig. 4 Cell viability of HepG2 cells (a and c) and 4T1 cells (b and d) after treatment with different concentrations of **ZZ-EDA** (a and b) or **ZZ-NN** (c and d). Photo-irradiation was carried out at 800 nm (9.15 mW cm^{-2} , 30 min).

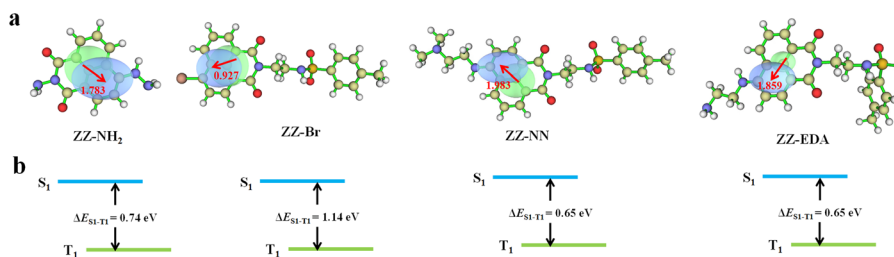


Fig. 3 (a) Electron-hole distributions seen in the S_1 states of **ZZ-NH₂**, **ZZ-Br**, **ZZ-NN**, and **ZZ-EDA**. The green and blue regions represent electron rich and electron deficient regions, respectively. (b) Schematic representation of the singlet state (S_1) and triplet state (T_1) energy levels of **ZZ-NH₂**, **ZZ-Br**, **ZZ-NN**, and **ZZ-EDA**, respectively, along with the corresponding energy differences.



viability values of $15.30\% \pm 0.16\%$ and $19.73\% \pm 0.27$ for the HepG2 and 4T1 cell lines, respectively. In contrast, the cell viability of HepG2 cells and 4T1 cells were 90% after treatment with the control molecules (**ZZ-Br** and **ZZ-NH₂**). We thus conclude that **ZZ-Br** and **ZZ-NH₂** have negligible effects on cell viability under otherwise identical conditions and concentrations (Fig. S25[†]). Meanwhile, the data showed when the concentration is $5.0 \mu\text{M}$, **ZZ-NN** produced cell viability values of $15.30\% \pm 0.16\%$ and $19.73\% \pm 0.27$ for the HepG2 and 4T1 cell lines, whereas protoporphyrin IX (PPIX, a known photosensitizer)³⁷ produced cell viability values of $36.51\% \pm 0.87\%$ and $33.59\% \pm 0.71$ for the HepG2 and 4T1 cell lines. And, due to its protonation ability, **ZZ-NN** has a certain selectivity to the acidic microenvironment of tumour cells, and also realizes the selective treatment of tumour cells to a certain extent. Then, a calcein-AM/PI double staining experiment³⁸ was performed to further assess the cytotoxicity of both **ZZ-NN** and **ZZ-EDA**. In this analysis, a green fluorescence at 500–530 nm (Calcein-AM) indicates living cells, while a red fluorescence at 600–630 nm (PI) reflects the presence of dead cells. As can be seen from an inspection of Fig. 5, only living cells with bright green fluorescence are observed when the cells were incubated with **ZZ-NN** and **ZZ-EDA** in the absence of photo-irradiation. However, under illumination (800 nm , using a femtosecond pulsed laser, 9.15 mW cm^{-2}), about 60% of the cells exhibit red fluorescence in the **ZZ-EDA** group, while nearly 100% exhibited red fluorescence in the **ZZ-NN** group (Fig. 5). These results are taken as evidence that with irradiation **ZZ-NN** and **ZZ-EDA** become lethal toward cells, with **ZZ-NN** being more photo-toxic than **ZZ-EDA**. This could be attributed to increased protonation of **ZZ-NN** over **ZZ-EDA**.

To confirm that the observed phototoxicity was due to a dual photochemical-biological effect, possible intracellular mechanisms were evaluated. And to support the experimental results in solution (Fig. 2d, S19 and S21[†]), the production of ROS in

living cells was investigated using 2, 7-dichlorodihydrofluorescein diacetate (DCFH-DA) as a ROS indicator and DHE as an $\text{O}_2^{\cdot-}$ indicator.^{14,39} As can be seen in Fig. 6, in all cases the cells exhibited strong fluorescence signals corresponding to ROS and $\text{O}_2^{\cdot-}$ production in the presence of **ZZ-NN** and **ZZ-EDA** with photo-irradiation (800 nm , 9.15 mW cm^{-2} , 3.0 min). However, analogous fluorescence signals were not observed to an appreciable extent in the absence of **ZZ-NN** and **ZZ-EDA** or when light alone was used. On this basis, we conclude that both **ZZ-NN** and **ZZ-EDA** produce $\text{O}_2^{\cdot-}$ when tested in cells. Taken in concert, these results thus provide evidence that **ZZ-NN** and **ZZ-EDA** can produce a type-I photochemical effect in cells as part of a dual-effect process.

The biological effects of **ZZ-NN** and **ZZ-EDA** were further investigated in living cells. Firstly, endocytosis inhibition experiments confirmed that **ZZ-NN** and **ZZ-EDA** enter cells through free diffusion (Fig. S27[†]). And the cell colocalization imaging showed the effective localization of **ZZ-NN** ($R = 0.95$) and **ZZ-EDA** ($R = 0.91$) in the lysosomes with a typical pH of approximately 5.0 (Fig. S28[†]). Under such acidic conditions, **ZZ-NN** and **ZZ-EDA** should have formed **ZZ-EDA-H⁺** and **ZZ-NN-H⁺** by protonation. Acridine orange (AO) staining was then used under conditions of photo-excitation, with the red fluorescence signal at 590–610 nm being used to monitor lysosomal integrity.⁴⁰ As shown in Fig. 7a, compared to HepG2 cells in the control and **ZZ-NN** groups, the red fluorescence disappeared in the **ZZ-NN + light** group, indicating lysosome rupture and subsequent cell death. However, some red fluorescence persisted in the **ZZ-EDA + light** group. This observation leads us to suggest that **ZZ-NN** may be used to destroy lysosomes effectively, while **ZZ-EDA** has a relatively weak destructive ability on lysosomes. This disparity is attributed to differences in the protonation propensities of **ZZ-NN** and **ZZ-EDA**. The higher basicity of **ZZ-NN** induces a stronger lysosomal proton sponge effect,³⁴ leading to a sharp change in H^+ concentrations in the

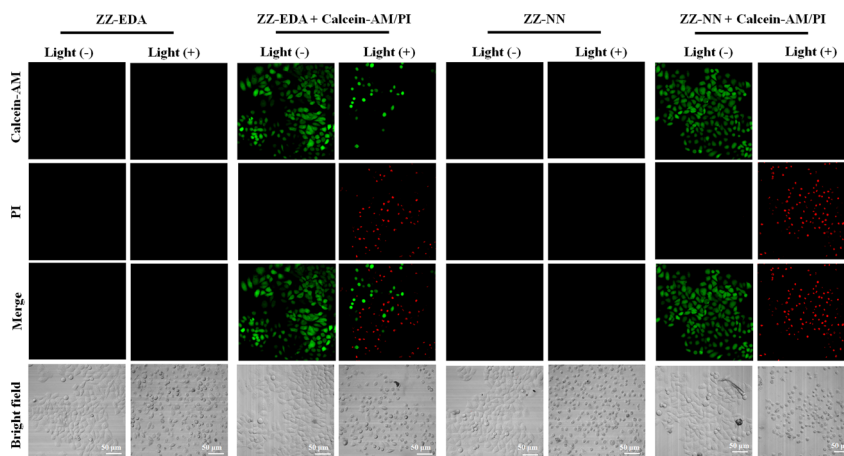


Fig. 5 Cell viability as determined *via* microscopic imaging analysis following staining with calcein AM/PI. HepG2 cells were treated with **ZZ-EDA** ($5.0 \mu\text{M}$) and **ZZ-NN** ($5.0 \mu\text{M}$) and irradiated at 800 nm (9.15 mW cm^{-2}) for 3.0 min . At this juncture, $2.0 \mu\text{M}$ of Calcein-AM (living cell marker) and $4.5 \mu\text{M}$ of PI (dead cell marker) were used to determine the cell viability, respectively. The Calcein-AM signal was monitored at 500–530 nm using 488 nm as the excitation wavelength. The corresponding wavelengths for PI were 600–630 nm and 488 nm . Note: as a control experiment, the fluorescence of **ZZ-EDA** and **ZZ-NN** were also monitored under the same conditions.



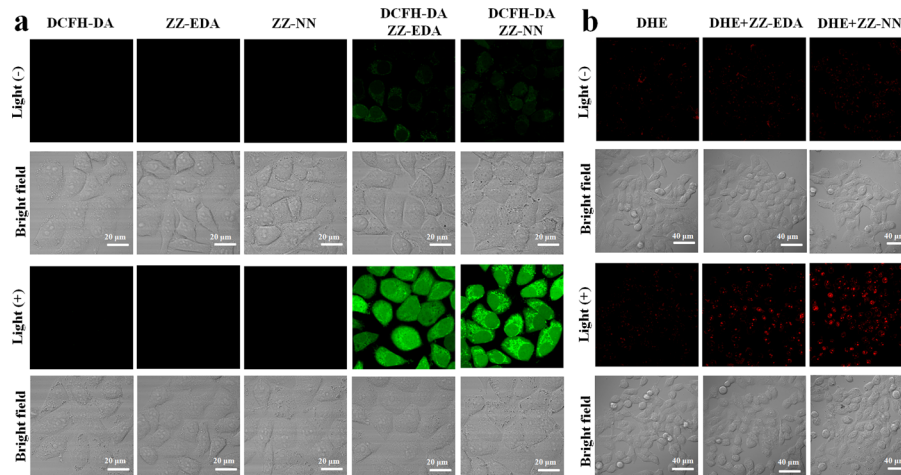


Fig. 6 (a) The ability of ZZ-EDA (5.0 μM) and ZZ-NN (5.0 μM) to produce ROS in HepG2 cells. Incubation times of 1.0 h were used. The irradiation light wavelength was 800 nm (9.15 mW cm^{-2} , 3.0 min). DCFH-DA (indicator for ROS) was used as a probe with a concentration of 6.0 μM . The DCFH-DA signal was monitored at 500–560 nm using 488 nm as the excitation wavelength. Note: as a control experiment, the fluorescence of ZZ-EDA and ZZ-NN were also monitored under the same conditions. (b) The ability of ZZ-EDA (5.0 μM) and ZZ-NN (5.0 μM) to produce $\text{O}_2^{\cdot-}$ in HepG2 cells. Incubation times of 1.0 h were used. The irradiation light wavelength was 800 nm (9.15 mW cm^{-2} , 3.0 min). DHE (indicator for $\text{O}_2^{\cdot-}$) was used as a probe concentration of 10 μM . The DHE signal was monitored at 590–630 nm using 530 nm as the excitation wavelength.

lysosome that ultimately causes its rupture (Fig. 7a). In other words, it is through protonation that ZZ-NN activates both the biological effect and strengthens the photochemical effect. Consequently, we speculate that compared to ZZ-EDA (IC_{50}), the relatively lower IC_{50} value (Fig. 4) of ZZ-NN for HepG2 and 4T1 cells originates from the stronger dual photochemical-biological effects.

To further visualize the impact of the proposed dual-effect on living cells, we conducted a mitochondrial membrane potential assessment using MitoProbe DiIC1(5) as an indicator for apoptosis.⁴¹ As shown in Fig. 7b, different degrees of

fluorescence reduction are correlated with decreased mitochondrial membrane potential in both the ZZ-NN + light and ZZ-EDA + light groups. However, a greater effect was seen in the ZZ-NN + light group when compared to the ZZ-EDA + light group. Notably, the mitochondrial membrane potential sharply declined in the ZZ-NN + light group after 6 min of irradiation, leading to almost complete disappearance of fluorescence and formation of microspheres within many cells. These results are taken as evidence that the dual photochemical-biological effect can lead to an amplified lethal response in cancer cells.

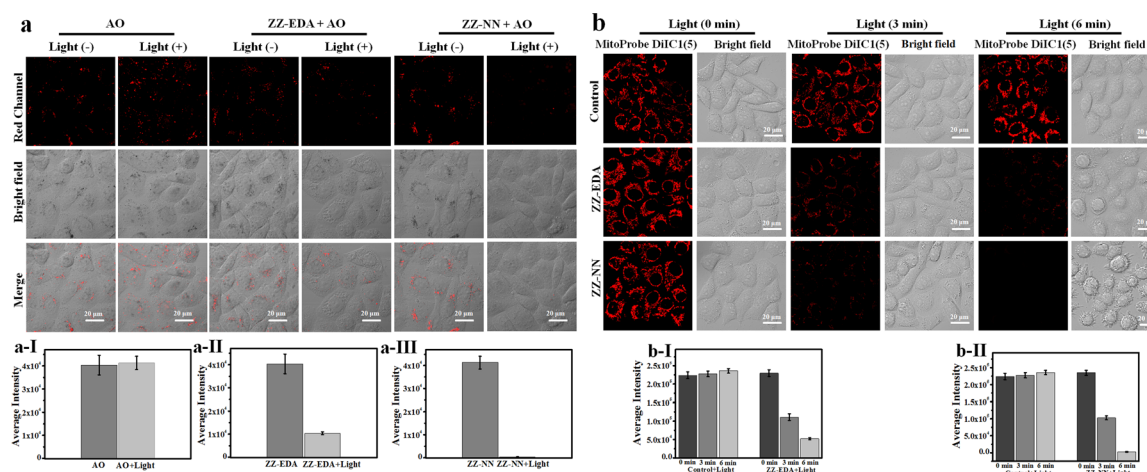


Fig. 7 (a) Lysosomal integrity in HepG2 cells as determined via microscopic imaging analysis using acridine orange (AO) staining. (a-I), (a-II) and (a-III) the signal intensity data statistics in (a). HepG2 cells were incubated with ZZ-EDA or ZZ-NN (5.0 μM each) for 1.0 h and irradiated using 800 nm light (9.15 mW cm^{-2} , 6.0 min). Then, 5.0 μM of AO was added. Signals in the red channel were monitored at 590–610 nm with 488 nm excitation. (b) Changes in the mitochondrial membrane potential for HepG2 cells. Confocal microscopic images of MitoProbe DiIC1(5) stained HepG2 cells under different conditions; (b-I) and (b-II) the signal intensity data statistics in (b). HepG2 cells were incubated with ZZ-EDA or ZZ-NN (5.0 μM each) for 1.0 h and irradiated at 800 nm (9.15 mW cm^{-2} , 6.0 min). Then, 5.0 μM of MitoProbe DiIC1(5) was added to monitor the mitochondrial membrane potential. Signals were monitored at 648–688 nm following 635 nm excitation.



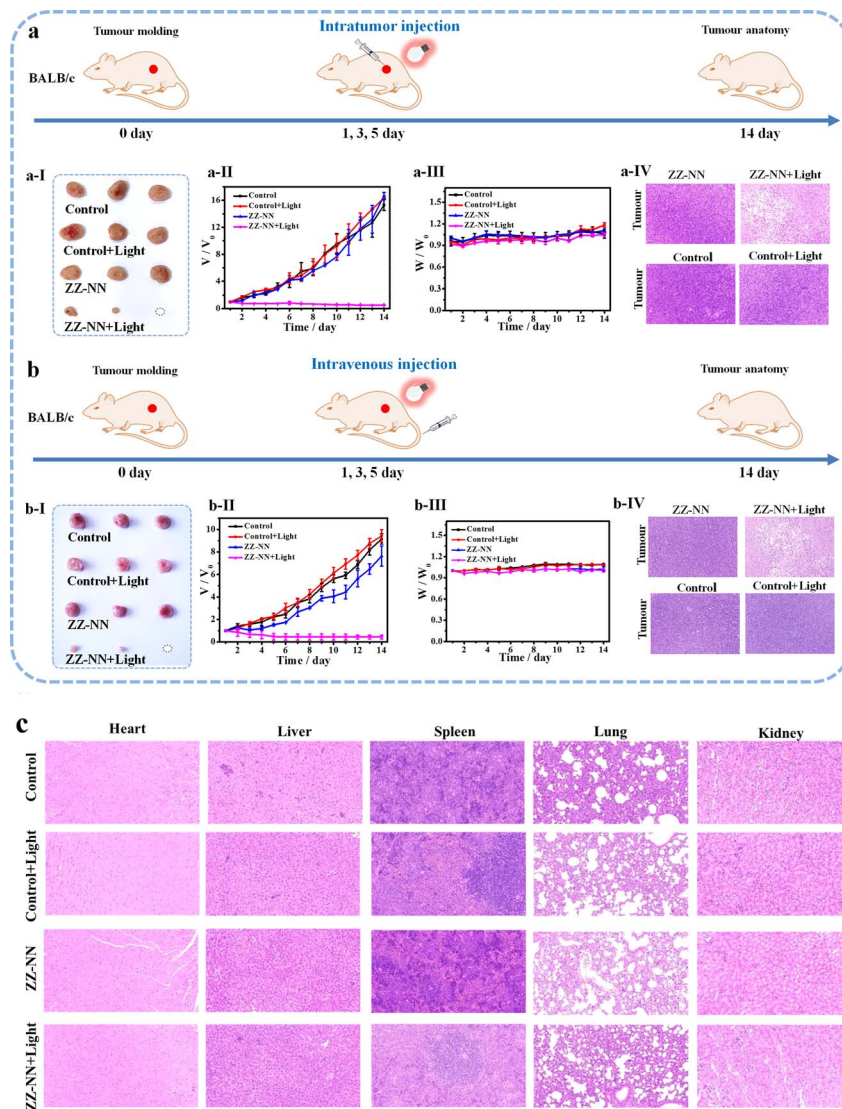


Fig. 8 Photo-induced therapeutic efficiency of ZZ-NN in 4T1 tumour-bearing BALB/c mice through (a) intratumour injection and (b) intravenous injection. ZZ-NN (1 mM, 20 μ L) and light were delivered at days 1, 3 and 5. Tumour volumes were measured one day apart and mice were weighed daily. Tumours were excised after 14 days and photographed. Changes in tumour size (a-I) and (b-I). Changes in tumour volume (a-II) and (b-II) seen for different groups (ZZ-NN group, ZZ-NN + light group, control group and control + light group) as monitored over 14 days. Note: due to individual differences in mice, the growth rate of tumours in (a) and (b) were different. (a-III) and (b-III) body weight changes of different groups (ZZ-NN group, ZZ-NN + light group, control group and control + light group) for 14 days. (a-IV) and (b-IV) H&E staining of the tumours of the mice after the various treatments. (c) H&E staining of the major organs (heart, liver, spleen, lung, and kidneys) of the mice after the various treatments.

Next, the anti-tumour efficacy of ZZ-NN was evaluated *in vivo*. A significant increase in the fluorescence signal of ZZ-NN (1.0 mM) was seen within 0–30 min, which then remained stable over an extended period in the 4T1 tumour-bearing mice model. The results from our anti-tumour study confirmed that exposure to light after injection of ZZ-NN led to almost complete eradication of tumours in mice whether administered *via* intratumour injection (Fig. 8a) or intravenous injection (Fig. 8b). In contrast, other experimental groups exhibited nearly identical (and high) rates of tumour growth (Fig. 8a, b and S30[†]). Hematoxylin-eosin (H&E) staining studies (Fig. 8a and b) also revealed tumour nucleus dissolution and apoptosis in the case of the ZZ-NN + light group. Furthermore, no

pathological changes were observed in key organs, such as the heart, liver, spleen, lungs and kidney. In addition, there was no significant change observed in the weight of mice across all treatment groups during the two-week experimental period (Fig. 8c). Collectively, these findings are taken as evidence that the proposed potent dual-action photochemical-biological effects of ZZ-NN translate into effective *in vivo* tumour growth inhibition.

Conclusions

In summary, we have developed a dual photochemical-biological strategy designed to enhance the therapeutic effect



of photosensitizers suitable for cancer treatment. This strategy combines a type-I photochemical effect and a cell-based proton sponge effect which was evaluated in this study using a small set of naphthalimide-based derivatives (photosensitizers (**ZZ-EDA** and **ZZ-NN**), protonated photosensitizers (**ZZ-EDA-H⁺** and **ZZ-NN-H⁺**) and control compounds (**ZZ-Br** and **ZZ-NH₂**)). Naphthalimide, as a traditional typical D- π -A type two-photon parent molecule, can enhance ISC through efficient charge separation to generate a type-I photochemical effect. Different weakly basic groups were covalently attached to improve the charge separation efficiency by protonation (proton sponge effect). **ZZ-NN-H⁺** exhibited enhanced O₂^{•-} production compared to that **ZZ-NN**, a result ascribed to protonation at pH = 5.0. When incubated with HepG2 cells this agent (5.0 μ M) induced a decrease in cell viability (to 15.30% \pm 0.16%) that was greater than that achieved by **ZZ-EDA** (48.37% \pm 0.30%). Similar results were observed in 4T1 cells (19.73% \pm 0.27%). Light irradiation caused destruction of lysosome integrity in cells treated with **ZZ-NN**. Finally, *in vivo* anti-tumour experiments confirmed the anti-tumour effects produced by **ZZ-NN** when subject to photo-irradiation, but not in its absence. Our work confirms the feasibility and advantages of design strategy that integrates the photochemical effect (*i.e.* type-I photochemical effect) with a biological effect (*i.e.* the proton sponge biological effect) for photosensitizers. Through this design approach, even traditional molecules such as naphthalimide-based derivatives can exhibit significant enhancement in their antitumour activity performance. The aforementioned strategy can thus be further expanded to facilitate the design of additional dyes for significantly enhancing antitumour activity.

Ethical statement

All animal experiments involved have been approved by the local research ethics review board of the Animal Ethics Committee of the Xinxiang Medical University (Henan, China, ethics statement Reference No. 2015016). And all the mice were used in accordance with institutional ethics committee regulations and guidelines on animal welfare.

Data availability

The authors confirm that the data supporting the findings of this study are available within the article [and/or its ESI†].

Author contributions

H. Y. N., J. L. S. and H. Z. proposed the concept and supervised the work; J. L. S., T. D. J. and H. Z. designed the experiments and wrote the paper; H. Y. N., J. L. S., T. D. J. and H. Z. contributed to the discussion and provided suggestions. Y. F. W., Y. L., Y. G. Y., G. W., H. Y. N., and H. Z. helped to analyse the data. All authors have discussed the results, drafted the manuscript and approved the final version of the manuscript.

Conflicts of interest

There are no conflicts to declare.

Acknowledgements

This work was supported by the National Natural Science Foundation of China (U21A20314, 22107089, 11974103, 21722501, 22378100); The work in Austin was supported by the National Institutes of Health-National Cancer Institute (grant CA68682 to J. L. S.) and the Robert A. Welch Foundation (F-0018 to J. L. S.). T. D. J. wishes to thank the University of Bath and the Open Research Fund of the School of Chemistry and Chemical Engineering, Henan Normal University (2020ZD01) for support. T. D. J. has been appointed as an Outstanding Talent by Henan Normal University. The work was supported by the Program for Innovative Research Team in Science and Technology in University of Henan Province (23IRTSTHN002).

Notes and references

- 1 M. Won, S. Koo, H. Li, J. L. Sessler, J. Y. Lee, A. Sharma and J. S. Kim, *Angew. Chem., Int. Ed.*, 2021, **60**, 3196–3204.
- 2 H. Y. Huang, B. L. Yu, P. Y. Zhang, J. J. Huang, Y. Chen, G. Gasser, L. N. Ji and H. Chao, *Angew. Chem., Int. Ed.*, 2015, **127**, 14255–14258.
- 3 W. P. Fan, P. Huang and X. Y. Chen, *Chem. Soc. Rev.*, 2016, **45**, 6488–6519.
- 4 S. K. Li, Q. L. Zou, Y. G. Li, C. Q. Yuan, R. R. Xing and X. H. Yan, *J. Am. Chem. Soc.*, 2018, **140**, 10794–10802.
- 5 B. Yuan, H. Wu, H. Wang, B. H. Tang, J. F. Xu and X. Zhang, *Angew. Chem., Int. Ed.*, 2021, **60**, 706–710.
- 6 A. Frei, R. Rubbiani, S. Tubafard, O. Blacque, P. Anstaett, A. Felgenträger, M. Tim, L. Spiccia and G. Gasser, *J. Med. Chem.*, 2014, **57**, 7280–7292.
- 7 X. j. Zhao, H. J. Zhao, S. Wang, Z. W. Fan, Y. Ma, Y. M. Yin, We. Wang, R. M. Xi and M. Meng, *J. Am. Chem. Soc.*, 2021, **143**, 20828–20836.
- 8 N. Niu, Y. Yu, Z. j. Zhang, M. M. Kang, L. Wang, Z. Zhao, D. Wang and B. Z. Tang, *Chem. Sci.*, 2022, **13**, 5929–5937.
- 9 D. Chen, Q. Xu, W. Wang, J. Shao, W. Huang and X. Dong, *Small*, 2021, **17**, 2006742–2006762.
- 10 M. Niedre, M. S. Patterson and B. C. Wilson, *Photochem. Photobiol.*, 2002, **75**, 382–391.
- 11 K. X. Teng, W. K. Chen, L. Y. Niu, W. H. Fang, G. L. Cui and Q. Z. Yang, *Angew. Chem., Int. Ed.*, 2021, **60**, 19912–19920.
- 12 S. K. Yao, Y. C. Chen, W. Z. Ding, F. W. Xu, Z. P. Liu, Y. H. Li, Y. P. Wu, S. M. Li, W. J. He and Z. J. Guo, *Chem. Sci.*, 2023, **14**, 1234–1243.
- 13 Y. L. Xu, C. L. Li, S. Lu, Z. Z. Wang, S. Liu, X. J. Yu, X. P. Li and Y. Sun, *Nat. Commun.*, 2022, **13**, 2009–2021.
- 14 J. An, S. L. Tang, G. B. Hong, W. Chen, M. M. Chen, J. T. Song, Z. L. Li, X. J. Peng, F. L. Song and W. H. Zheng, *Nat. Commun.*, 2022, **13**, 2225–2234.
- 15 H. Shigemitsu, K. Ohkubo, K. Sato, A. Bunno, T. Mori, Y. Osakada, M. Fujitsuka and T. Kida, *JACS Au*, 2022, **2**, 1472–1478.



- 16 K. X. Teng, L. Y. Niu and Q. Z. Yang, *J. Am. Chem. Soc.*, 2023, **145**(7), 4081–4087.
- 17 M. J. Mitchell, M. M. Billingsley, R. M. Haley, M. E. Wechsler, N. A. Peppas and R. Langer, *Nat. Rev. Drug Discovery*, 2021, **20**, 101–124.
- 18 B. Ballarín-González and K. Howard, *Adv. Drug Delivery Rev.*, 2012, **64**, 1717–1729.
- 19 L. L. Shi, W. B. Wu, Y. K. Duan, L. Xu, Y. Y. Xu, L. D. Hou, X. J. Meng, X. Y. Zhu and B. Liu, *Angew. Chem., Int. Ed.*, 2020, **59**, 19168–19174.
- 20 C. Donohoe, M. O. Senge, L. G. Arnaut and L. C. Gomes-da-Silva, *Biochim. Biophys. Acta, Rev. Cancer*, 2019, **1872**(2), 188308–188324.
- 21 P. Zhang, T. Y. Wang, H. M. Xiong and J. L. Kong, *Talanta*, 2014, **127**, 43–50.
- 22 M. Yezhelyev, L. F. Qi, R. O'Regan, S. M. Nie and X. H. Gao, *J. Am. Chem. Soc.*, 2008, **130**, 9006–9012.
- 23 Y. Yamazaki, M. Nango, M. Matsuura, Y. Hasegawa, M. Hasegawa and N. Oku, *Gene Ther.*, 2000, **7**, 1148–1155.
- 24 H. W. Duan and S. Nie, *J. Am. Chem. Soc.*, 2007, **129**, 3333–3338.
- 25 M. E. Guicciardi, M. Leist and G. J. Gores, *Oncogene*, 2004, **23**(16), 2881–2890.
- 26 C. J. Luke, S. C. Pak, Y. S. Askew, *et al.*, *Cell*, 2007, **130**(6), 1108–1119.
- 27 S. S. Zhang, W. F. Yang, X. Lu, X. Y. Zhang, Z. C. Pan, D. H. Qu, D. Mei, J. Mei and H. Tian, *Chem. Sci.*, 2023, **14**, 7076–7085.
- 28 S. S. Liu, G. X. Feng, B. Z. Tang and B. Liu, *Chem. Sci.*, 2021, **12**, 6488.
- 29 Y. F. Xiao, W. C. Chen, J. X. Chen, G. H. Lu, S. Tian, X. Cui, Z. Zhang, H. Chen, Y. P. Wan, S. L. Li and C. S. Lee, *ACS Appl. Mater. Interfaces*, 2022, **14**, 5112–5121.
- 30 A. M. Kaufmann and J. P. Krise, *J. Pharm. Sci.*, 2007, **96**, 729–746.
- 31 X. Xiao, I. Kurganskii, P. Maity, J. Z. Zhao, X. Jiang, O. F. Mohammed and M. Fedin, *Chem. Sci.*, 2022, **13**, 13426–13441.
- 32 Y. B. Wang, S. D. Xu, L. L. Shi, C. Teh, G. B. Qi and B. Liu, *Angew. Chem., Int. Ed.*, 2021, **60**, 14945–14953.
- 33 Lu. Zhang, F. L. Jiang, Q. L. Guo, Y. Liu and P. Jiang, *Anal. Chem.*, 2022, **94**, 4126–4133.
- 34 R. J. Christie, N. Nishiyama and K. Kataoka, *Endocrinol.*, 2010, **151**(2), 466–473.
- 35 Y. J. Hong, W. H. Geng, T. Zhang, G. S. Gong, C. Y. Li, C. Z. Zheng, F. Liu, J. Qian, M. Chen and B. Z. Tang, *Angew. Chem., Int. Ed.*, 2022, **61**, e202209590.
- 36 S. S. Razi, Y. H. Koo, W. Kim, W. B. Yang, Z. J. Wang, H. Gobeze, F. D'Souza, J. Z. Zhao and D. Kim, *Inorg. Chem.*, 2018, **57**, 4877–4890.
- 37 Z. Hussain, Q. Qi, J. J. Zhu, K. E. Anderson and X. C. Ma, *Pharmacol. Ther.*, 2023, **248**, 108487.
- 38 Y. Y. Zhao, L. Zhang, Z. X. Chen, B. Y. Zheng, M. R. Ke, X. S. Li and J. D. Huang, *J. Am. Chem. Soc.*, 2021, **143**, 13980–13989.
- 39 C. F. Wang, Y. J. Sun, S. J. Huang, Z. X. Wei, J. Y. Tan, C. F. Wu, Q. Chen and X. J. Zhang, *J. Am. Chem. Soc.*, 2023, **145**, 13099–13113.
- 40 W. Li, S. L. Yin, Y. Shen, H. Y. Li, L. Yuan and X. B. Zhang, *J. Am. Chem. Soc.*, 2023, **145**, 3736–3747.
- 41 J. C. Gomez-Sanchez, M. Delgado-Esteban, I. Rodriguez-Hernandez, T. Sobrino, N. Perez de la Ossa, S. Reverte, J. P. Bolaños, R. Gonzalez-Sarmiento, J. Castillo and A. Almeida, *J. Exp. Med.*, 2011, **208**(3), 429–437.

